ACS APPLIED MATERIALS & INTERFACES

Research Article

www.acsami.org

Solution-Processed Ga-Doped ZnO Nanorod Arrays as Electron Acceptors in Organic Solar Cells

Riski Titian Ginting,[†] Chi Chin Yap,*[,†] Muhammad Yahaya,[†] and Muhammad Mat Salleh[‡]

[†]School of Applied Physics, Faculty of Science and Technology, Universiti Kebangsaan Malaysia, 43600 UKM Bangi, Selangor, Malaysia

[‡]Institute of Microengineering and Nanoelectronics (IMEN), Universiti Kebangsaan Malaysia, 43600 UKM Bangi, Selangor, Malaysia

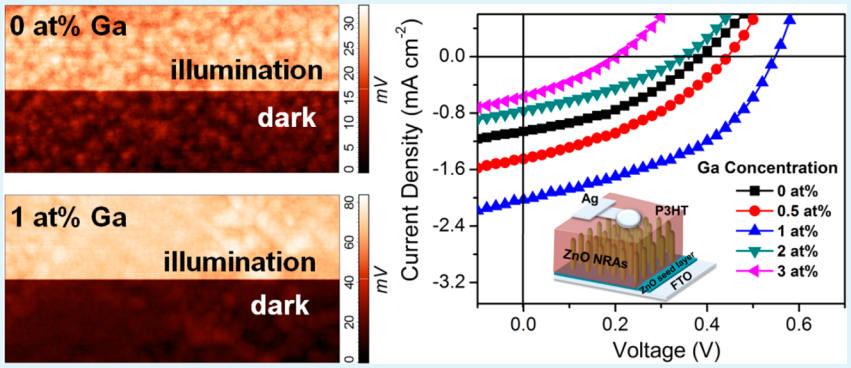

ABSTRACT: This paper reports the utilization of ZnO nanorod arrays (NRAs) doped with various concentrations of Ga (0, 0.5, 1, 2, and 3 at %) as electron acceptors in organic solar cells. The donor, poly(3-hexylthiophene) (P3HT), was spin coated onto Ga-doped ZnO NRAs that were grown on fluorine-doped tin oxide (FTO) substrates, followed by the deposition of a Ag electrode by a magnetron sputtering method. Adjusting the Ga precursor concentration allowed for the control of the structural and optical properties of ZnO NRAs. The short circuit current density increased with increasing Ga concentration from 0 to 1 at %, mainly because of improved exciton dissociation and increased charge extraction. Meanwhile, the reduced charge recombination and lower hole leakage current led to an increase in the open circuit voltage with Ga concentrations up to 1 at %. The device with the optimum Ga concentration of 1 at % exhibited power conversion efficiency nearly three times higher compared to the device without Ga doping. This finding suggests that the incorporation of Ga can be a simple and effective approach to improve the photovoltaic performance of organic solar cells.

KEYWORDS: *doping, charge recombination, electron acceptor, exciton dissociation, organic solar cells, ZnO nanorod arrays*

INTRODUCTION

Over the past few years, bulk heterojunction organic solar cells (OSCs) have become promising because of their light weight, flexibility, low manufacturing costs, and environmentally friendly characteristics.[1,2] Hole conducting polymers including poly(3-hexylthiophene) (P3HT) and C_{60} derivatives such as (6,6)-phenyl C61 butyric acid methyl ester (PCBM), have been widely used as donors and acceptors, respectively, in bulk heterojunction OSCs.[3−5] Generally, a nanoscale phase separation between the donor and acceptor is required to provide a large interfacial area for efficient exciton dissociation because the exciton diffusion length is small. However, a discontinuous transport pathway for the separated charge carriers to reach the collecting electrodes normally occurs under such conditions, hence leading to less charge carriers extracted from the device.[6] The phase separation in the blend layer needs to be optimized to obtain balanced exciton dissociation and charge transport. It has been reported that the phase separation of P3HT and PCBM is highly dependent on the processing condition and is thus difficult to control precisely.[7−9]

One-dimensional vertically aligned metal oxide nanostructures, such as ZnO nanorod arrays (NRAs), are considered suitable candidates for replacing PCBM as electron acceptors because they can provide a direct pathway for the electron transport after the exciton dissociation.[10−12] More importantly, the desired size, density and interspacing of ZnO NRAs can be easily obtained by a low temperature chemical bath deposition method.[13,14] Despite the advantages of ZnO NRAs, the power conversion efficiency (PCE) of OSCs based on P3HT and ZnO NRAs is still much lower than that based on P3HT and PCBM.[15,16] It is believed that small interfacial areas between P3HT and ZnO NRAs as well as the charge recombination caused by the defects appearing on the surface of the ZnO contribute to the poor photovoltaic performance.[10,16,17]

Received: February 6, 2014
Accepted: March 17, 2014
Published: March 17, 2014

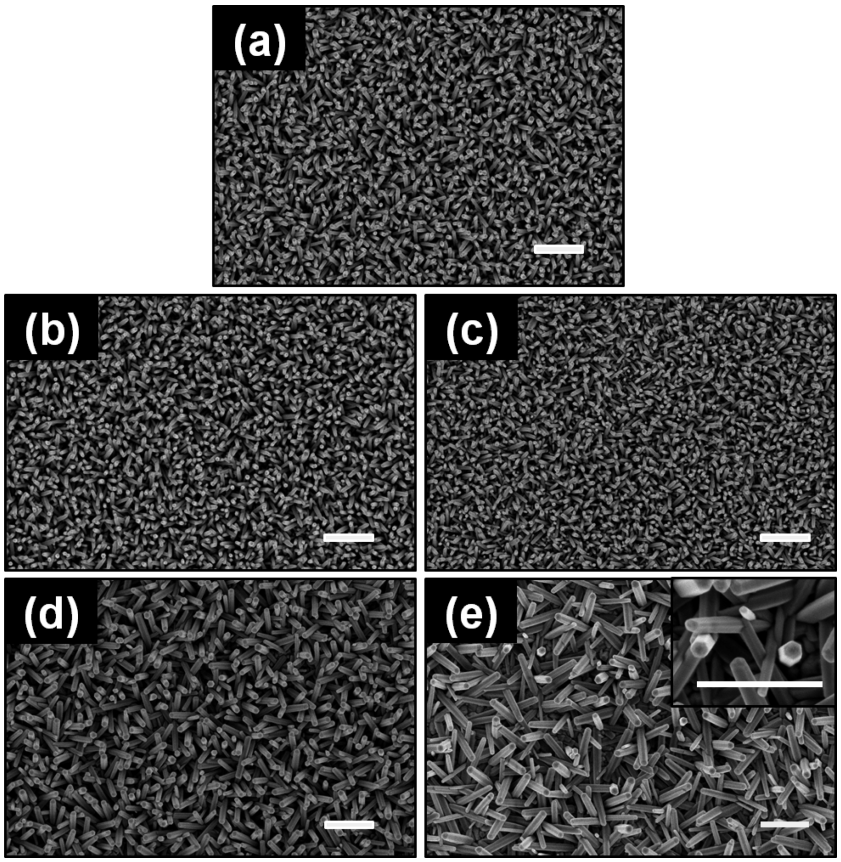

Figure 1. FESEM top-view images of the ZnO NRAs with Ga doping concentration of (a) 0 at %, (b) 0.5 at %, (c) 1 at %, (d) 2 at %, and (e) 3 at %. Inset shows the higher magnification of the 5 at% Ga-doped ZnO NRAs. Scale bar is 500 nm.

Although dense ZnO NRAs with a high surface-to-volume ratio may have a large exposed surface area, the effective interfacial area for exciton dissociation is normally limited as a result of poor infiltration of P3HT into the small interspacing between the ZnO NRAs.[10,11,13] In addition, ZnO nanorods with a large surface area normally contain more surface defects, which act as recombination centers for charge carriers.[18,19] Therefore, it is important to find a simple approach to obtain ZnO NRAs with high a surface-to-volume ratio while maintaining good infiltration of P3HT and low surface defects.

Ruankham et al. reported that the effective exciton dissociation at the ZnO nanorod-P3HT interfaces as a result of the oxygen-enriched ZnO surface could be achieved by doping an appropriate amount of Li into the ZnO NRAs.[16] However, the dependence of the ZnO nanorod morphology on the doping concentration of Li was not explored. More recently, our work showed that high density and large surface-to-volume ratio ZnO NRAs with low oxygen defects could be obtained by introducing an optimum amount of Mg dopant.[20] The PCE improved significantly compared to that without the Mg doping because of the high interfacial areas for efficient exciton dissociation and suppression of charge recombination. Although Ga-doped ZnO NRAs and thin films have recently been used as electron transport layers in OSCs,[21−23] there has been no investigation into the application of Ga-doped ZnO NRAs as electron acceptors in OSCs. In the present work, the effects of the Ga doping concentration (0, 0.5, 1, 2, and 3 at %) on the structural and optical properties of ZnO NRAs and the subsequent photovoltaic performance of fluorine-doped tin oxide (FTO)/Ga-doped ZnO NRAs/P3HT/Ag devices have been investigated. The increment of the short circuit current density (J_{sc}) with an increase in the Ga concentration from 0 to 1 at % can be attributed to increased interfacial area for exciton dissociation and improved charge extraction. Additionally, the increase in the open circuit voltage (V_{oc}) correlates with the reduced charge recombination at the interface of ZnO and P3HT, as well as the lower hole leakage current. The 1 at% Ga-doped device exhibited nearly a three-fold increase in PCE compared to the device without Ga doping.

EXPERIMENTAL METHOD

The ZnO NRAs were synthesized using a two-step solution method.[24,25] The first step involved the deposition of a ZnO seed layer on a pre-cleaned FTO glass substrate by spin coating an equimolar solution of 0.2 M zinc acetate dehydrate ($Zn(CH_3COO)_2 \cdot (H_2O)_2$) and diethanolamine in ethanol at 3000 rpm for 40 s. The process was repeated three times and the samples were then annealed at 300 °C for 1 h. The ZnO NRAs were subsequently grown by suspending the seed layer-coated substrates in an equimolar aqueous solution of 40 mM zinc nitrate hexahydrate ($Zn(NO_3)_2 \cdot 6H_2O$) and hexamethylenetetramine (HMT) at 90 °C for 45 min in a laboratory oven. The gallium nitrate ($Ga(NO_3)_3 \cdot xH_2O$), with different atomic ratios (0, 0.5, 1, 2, and 3 at %) relative to $Zn(NO_3)_2 \cdot 6H_2O$, was added to the growth solutions. To fabricate the devices, a solution of P3HT (Rieke Metals) at a concentration of 40 mg/mL dissolved in chlorobenzene was spin-coated onto the ZnO NRAs at 1500 rpm for 60 s. Finally, without further annealing, the Ag anode was subsequently deposited by magnetron sputtering. The thickness of the Ag electrode was approximately 150 nm and the active area defined by mask was 0.07 cm^2.

The surface morphology of the ZnO NRAs with various Ga concentrations ranging from 0 to 3 at % was characterized by field

dx.doi.org/10.1021/am5007832 | ACS Appl. Mater. Interfaces 2014, 6, 5308−5318

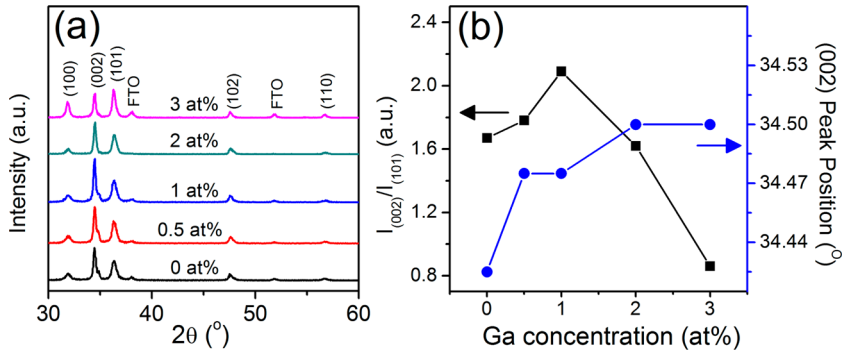

Figure 2. (a) XRD spectra of ZnO NRAs with different Ga doping concentrations. (b) The intensity ratio of the (002) to the (101) diffraction peaks and the (002) diffraction peak position as a function of Ga concentration.

emission scanning electron microscopy (FESEM, Hitachi SU8000). The crystal structures of the ZnO NRAs were studied by X-ray diffraction (XRD, Bruker AXS D8 Advance). The thickness of the ZnO NRAs was measured by means of a Veeco M6 surface profiler. The chemical compositions of the ZnO NRAs were measured by X-ray photoelectron spectroscopy (XPS, Kratos/Shimadzu Axis Ultra DLD) with a monochromatic Al Kα radiation source at room temperature. The optical absorption spectra of the ZnO NRAs and ZnONRAs/P3HT films were recorded using a Perkin Elmer Lambda 900 UV−vis spectrometer. The steady-state photoluminescence (PL) spectra of the ZnO NRAs and ZnO NRAs/P3HT films were investigated at excitation wavelengths of 300 and 472 nm, respectively, using an Edinburg FLS920 spectrophotometer. The same spectrophotometer equipped with a 472.4 nm picosecond laser diode as an excitation source was used to obtain the time-resolved photoluminescence (TRPL) spectra of P3HT coated on the ZnO NRAs. The J–V characteristics of the devices were measured using a Keithley 237 SMU under the illumination of a solar simulator (Newport 96000, 150 W) at 100 mW cm^{-2} equipped with an AM 1.5G filter and under dark conditions. The atomic force microscopy (AFM) topography and the corresponding surface potential images of the ZnONRAs/P3HT films were obtained using an NT-MDT Ntegra Prima AFM under dark and illumination conditions of a halogen lamp (Quartzline, 150 W) in ambient air. The silicon cantilever with a PtIr conductive coating (NSG-01/Pt, NT-MDT) was driven at a frequency of 146 kHz, and the tip-sample surface distance was kept constant at 10 nm. The charge extraction by linearly increasing voltage (CELIV) technique[26] was performed under dark conditions using a Siglent SDG 1020 function generator to apply a voltage pulse from −0.4 to 3.5 V with a slope of 0.05 V μs^{-1}, and the dynamic response of the mobile carrier extraction was recorded simultaneously from the load of a 50 Ω resistor in series with the device by a digital oscilloscope (Siglent 1103CM). The impedance measurements of the devices were performed in dark conditions using an Ivium Vertex potentiostat with frequency up to 1 MHz at different applied bias voltages and a low AC oscillating voltage of 30 mV. Iviumsoft Electrochemistry software was used to fit the obtained spectra. For the transient photovoltage measurements, the devices were characterized at an open circuit condition under illumination from the solar simulator.[27] A small perturbation of V_{oc} was generated by a pulse from a green collimated light emitting diode (LED) (505 nm, repetition rate = 1 kHz, pulse width = 100 μs), and the decay of the photovoltage was recorded by a high impedance digital oscilloscope (Siglent 1103CM). All device preparation, fabrication, and measurements were conducted under ambient conditions.

RESULTS AND DISCUSSIONS

Figure 1 shows the FESEM top-view images of the ZnO NRAs with different Ga doping concentrations ranging from 0 to 3 at %. The average diameter of the nanorods decreased slightly from 36 to 31 nm, whereas the density increased from 150 to 220 rods μm^{-2} with increasing Ga concentration up to 1 at %. Meanwhile, the average thickness of the ZnO NRAs layer increased from 235 to 284 nm, suggesting that longer nanorods were obtained. The introduction of the Ga dopant at a relatively low concentration might promote the growth of ZnO NRAs along the c-axis direction as previously reported.[28,29] However, a different behavior was observed when the concentration of Ga was raised to 2 and 3 at %. The average diameter increased to 62 and 82 nm, whereas the density of the nanorods decreased sharply to 80 and 40 rods μm^{-2} for 2 and 3 at % Ga-doped samples, respectively. It is believed that the Ga precursor added to the growth solution might interact with OH^- ions released by HMT to form complexes.[28,30] The reduction of OH^- ions limits the heterogeneous nucleation of ZnO in the early stage of the growth process, resulting in a lower number of nucleation sites for nanorod growth. In addition, the lateral growth of ZnO is not effectively hindered at lower nucleation densities, allowing large-diameter ZnO NRAs to be obtained. Because the nanorods were not well aligned vertically as a result of the rough underlying ZnO seed layer-coated FTO surface, the adjacent nanorods with large diameters have a greater possibility of intersecting at the early growth stage. As a result, the growing process of some of the nanorods might terminate and lead to a further decrease in the nanorod density. The present findings closely agree with the previous reports, in which the morphology of the ZnO NRAs could be controlled by tuning the Ga precursor concentration in the growth solution.[28,29]

XRD spectra of the ZnO NRAs with different Ga doping concentrations grown on top of FTO substrates are shown in Figure 2a. All the diffraction peaks from the undoped and Ga-doped ZnO NRAs could be indexed to the hexagonal wurtzite structure of ZnO (JCPDS No. 36-1451). The (002) diffraction peak dominated the XRD spectra for all the samples except for the sample doped with 3 at % Ga, indicating that the favored growth direction of the ZnO NRAs was along the c-axis. Figure 2b shows the intensity ratio of the (002) to the (101) diffraction peaks and the (002) diffraction peak position as a function of the Ga doping concentration. The intensity ratio gradually increased with increasing Ga concentration from 0 to 1 at % but dropped noticeably when the Ga concentration was raised to 2 and 3 at %, implying that the ZnO NRAs doped with high concentrations of Ga were no longer highly oriented along the c-axis. This observation is in good agreement with the FESEM results shown above (Figure 1). It is important to note that no Ga characteristic peaks or other crystalline phases were observed in the XRD spectra of the Ga-doped samples. Furthermore, the (002) diffraction peak shifted slightly toward

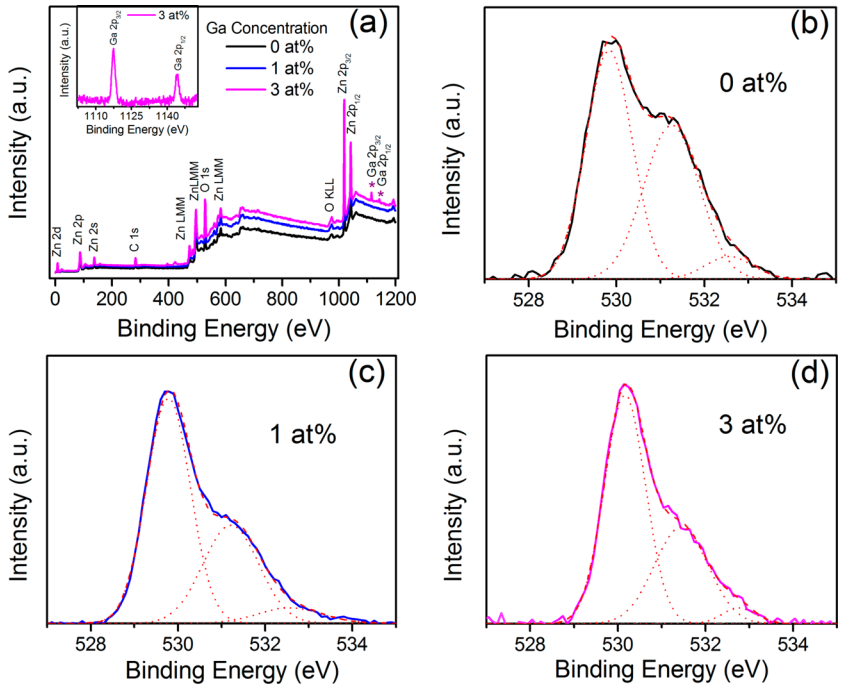

Figure 3. (a) Wide-scan XPS spectra of the ZnO NRAs with various Ga concentrations. The inset shows the narrow-scan XPS spectrum of Ga 2p peaks for 3 at% Ga-doped ZnO NRAs. The narrow-scan XPS spectra and deconvoluted curves of the O1s peak for the (b) 0, (c) 1, and (d) 3 at% Ga-doped ZnO NRAs.

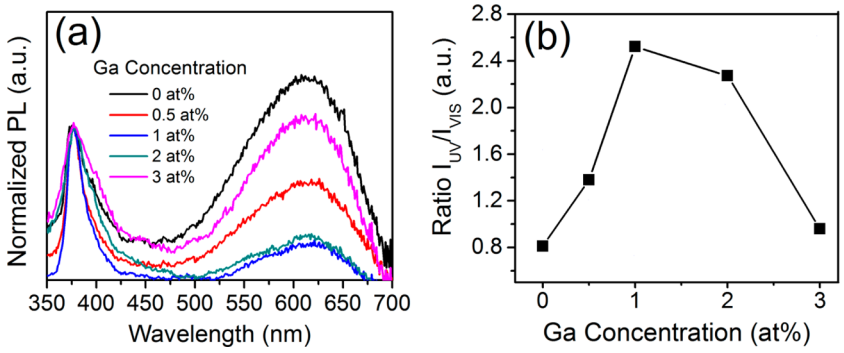

Figure 4. (a) Normalized PL spectra of the ZnO NRAs with various Ga doping concentrations with an excitation wavelength of 300 nm. (b) The ratio of UV to visible emission peaks as a function of Ga concentration.

a higher angle as the Ga concentration increased. This observation suggests that the Ga ions were successfully incorporated into the ZnO lattice by substituting the Zn^{2+} sites because the ionic radius of Ga^{3+} (0.62 Å) is smaller than that of Zn^{2+} (0.74 Å).[31]

To obtain the chemical composition of the Ga-doped ZnO NRAs and the chemical state of the Ga in the ZnO nanorod, XPS measurements were performed. Figure 3a demonstrates the typical wide-scan XPS spectra of the 0, 1, and 3 at % Ga-doped ZnO NRAs. The peak positions were referenced to the carbon impurity (C 1s) at a binding energy of 284.5 eV. Strong signals of Zn and O were clearly observed for all the tested samples. Meanwhile, weak peaks attributed to the Ga 2p core level were also detected for 3 at % Ga-doped ZnO NRAs. From the inset of Figure 3a, the two peaks located at 1117.3 and 1144.2 eV are attributed to the electronic states of Ga $2p_{3/2}$ and Ga $2p_{1/2}$, respectively. The peak positions are close to the reported values for a Ga^{3+} state,[28,30] providing further evidence that some of the Zn^{2+} sites in the ZnO lattice have been replaced by the Ga^{3+} ions. The quantitative analysis reveals that the Ga content in the ZnO NRAs was 2.13 at % when 3 at % Ga precursor was added to the growth solution. However, the Ga peaks were not found in the wide XPS spectrum of the 1 at % Ga-doped sample within the detection limit of the instrument, possibly a result of the small amount of Ga dopant.[32] Figures 3b-d depict the narrow-scan XPS spectra of the O1s peak of the 0, 1, and 3 at % Ga-doped ZnO NRAs and their respective deconvolution results. The asymmetric O1s peaks could be deconvoluted into three separate peaks with low, medium and high binding energies by Gaussian fitting.[33] The low binding energy component could be ascribed to the bonding between O^{2-} and Zn^{2+} (or Ga^{3+}) ions in the ZnO lattice.[34] The peak of the low binding energy component shifted slightly from ~528.85 to ~530.13 eV, with an increasing Ga doping concentration up to 3 at %. The increase in the binding energy could be attributed to the larger electronegativity of Ga^{3+} compared to Zn^{2+}.[30] In addition, the medium binding energy component centered at 531.1 eV could be related to the O^{2-} ions in the oxygen-deficient regions within the ZnO matrix.[35] It can be clearly seen that the intensity of the

dx.doi.org/10.1021/am5007832 | ACS Appl. Mater. Interfaces 2014, 6, 5308−5318

medium binding energy component significantly decreased with the introduction of the Ga dopant, suggesting a significant reduction in the oxygen defects on the ZnO surfaces. The component with the high binding energy centered at approximately 532.6 eV, which is usually associated with the chemically adsorbed oxygen, free oxygen atom or OH^- radicals on the surface of ZnO, remained nearly unchanged upon the incorporation of Ga.[28,36]

The normalized room temperature PL spectra of the ZnO NRAs with different Ga doping concentrations are shown in Figure 4a. All the PL spectra consisted of two bands, a UV band centered at ~377 nm corresponding to the near band edge emission and a broad visible band in the range of 500−700 nm. The broad visible band is usually related to the presence of structural defects and impurities,[25] such as zinc vacancy, oxygen vacancy, oxygen atom at the zinc position in the crystal lattice, zinc atom at the oxygen position in the crystal lattice, oxygen interstitial, and zinc interstitial. It is believed that the broad yellow emission (peaked at 610 nm) in the present work originated from the oxygen interstitial, which is commonly reported for ZnO NRAs synthesized by hydrothermal methods.[25,37] Although all the samples exhibited UV and visible emissions at similar positions, a significant difference in the ratio of UV to visible emissions was detected (Figure 4b). The UV to visible emission ratio increased significantly when the Ga concentration was raised from 0 to 1 at %. The decrease in the broad yellow emission is consistent with the XPS results, which indicates that Ga doping might reduce the number of defects induced by oxygen interstitial. However, a further increase in the Ga concentration to 2 and 3 at % resulted in a lower UV to visible emission ratio, revealing that the dopant-related visible emission began to play a role at the high doping concentration.[28,30]

Current density−voltage (J−V) characteristics of the devices with different Ga doping concentrations ranging from 0 to 3 at % under illumination are shown in Figure 5. The series resistance (R_s) and shunt resistance (R_{sh}) were estimated from the inverse slope at V_{oc} and J_{sc} in the J−V curve, respectively. The J_{sc}, V_{oc}, and fill factor (FF) increased with increasing Ga concentration from 0 to 1 at%, and then decreased when the Ga concentration exceeded 1 at %. The highest PCE of 0.44 ± 0.04% was achieved at the optimum Ga concentration of 1 at %, with a J_{sc} of 1.98 ± 0.07 mA cm^{-2}, a V_{oc} of 0.53 ± 0.02 V, and an FF of 0.42 ± 0.02. The PCE of the optimum device is nearly three times greater than that of the device without doping. The average photovoltaic parameter data with their respective standard deviations of four individual devices for each sample are summarized in Table 1.

It is well known that the J_{sc} is dependent on the light absorption, exciton dissociation, charge transport, and charge collection at the electrodes.[38−41] Because the P3HT deposition condition was the same for all the devices, the light absorption of the photoactive material in all the devices should also remain unchanged. This can be proven by the similar optical absorption spectra of the undoped and Ga-doped ZnO NRAs/P3HT films, as depicted in Figure 6. To determine whether the change in J_{sc} is related to the exciton dissociation behavior at the ZnO/P3HT interface, steady-state PL and TRPL measurements were performed. The steady-state PL spectra of the undoped and Ga-doped ZnO NRAs/P3HT films are shown in Figure 7a. The PL spectra exhibited a main peak at 725 nm with a shoulder emission at approximately 655 nm, corresponding to the typical PL emission of P3HT.[42] It can be clearly seen that the PL intensity of the P3HT coated on 1 at% Ga-doped ZnO NRAs reduced remarkably compared to that coated on undoped sample. The PL quenching could serve as an indicator for effective exciton dissociation at the interfaces.[20,39] Similar behavior was observed in the TRPL decay curves, as shown in Figure 7b. The PL decay was fitted using a bi-exponential function. The P3HT coated on 0.5 and 1 at % Ga-doped ZnO NRAs exhibited shorter average decay lifetimes of 563 and 537 ps, respectively, in comparison to that coated on undoped ZnO NRAs (604 ps). The faster PL decay

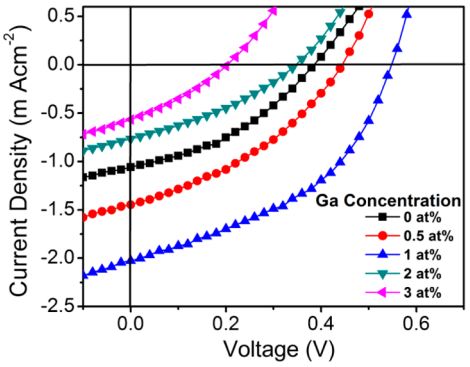

Figure 5. J−V curves of the devices with different Ga concentrations under illumination.

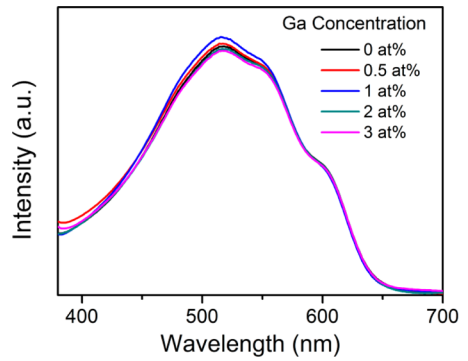

Figure 6. Optical absorption spectra of the undoped and Ga-doped ZnO NRAs/P3HT films.

Table 1. Photovoltaic Parameters of Devices with Different Ga Concentration

Ga concentration (at %)	J_{sc} (mA cm^{-2})	V_{oc} (V)	FF	PCE (%)	R_s (Ω cm^2)	R_{sh} (Ω cm^2)
0	1.02 ± 0.06	0.41 ± 0.03	0.35 ± 0.03	0.15 ± 0.01	254 ± 49	908 ± 64
0.5	1.55 ± 0.09	0.46 ± 0.02	0.40 ± 0.01	0.28 ± 0.03	114 ± 10	960 ± 72
1	1.98 ± 0.07	0.53 ± 0.02	0.42 ± 0.02	0.44 ± 0.04	46 ± 13	1190 ± 96
2	0.74 ± 0.06	0.34 ± 0.01	0.35 ± 0.02	0.09 ± 0.01	249 ± 46	848 ± 80
3	0.56 ± 0.02	0.23 ± 0.05	0.32 ± 0.01	0.04 ± 0.01	275 ± 40	606 ± 99

dx.doi.org/10.1021/am5007832 | ACS Appl. Mater. Interfaces 2014, 6, 5308−5318

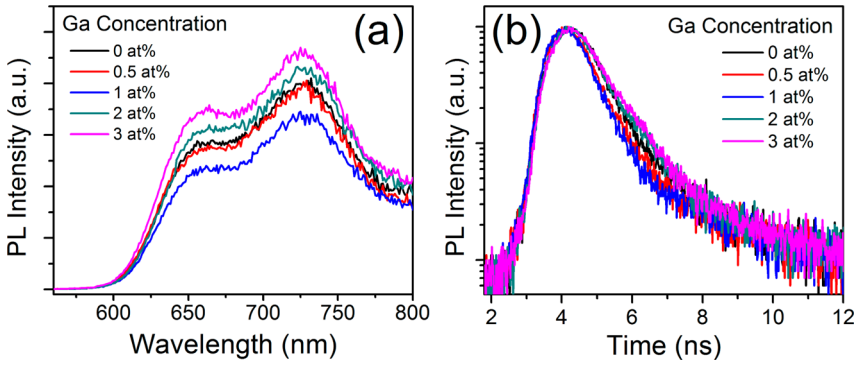

Figure 7. (a) Steady-state PL and (b) TRPL decay curves of P3HT coated on ZnO NRAs with different Ga doping concentrations.

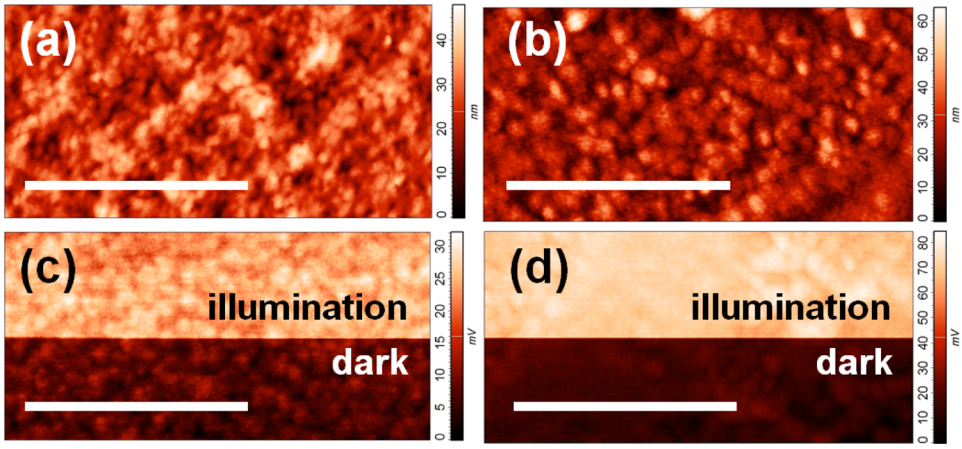

Figure 8. AFM topography and surface potential images of P3HT coated on (a, c) undoped and (b, d) 1 at % Ga-doped ZnO NRAs. Scale bars are 4 μm.

could be correlated with the formation of high-density, long and small-diameter ZnO NRAs, which offer a larger interfacial area for exciton dissociation.[20] As the Ga concentration increased above 1 at %, the PL intensity, and PL decay lifetime of P3HT were even higher than those of the sample without doping. This result can be explained by the poor exciton dissociation as a result of the smaller interfacial area between P3HT and the low-density ZnO nanorods with large diameters. This observation is consistent with the FESEM results discussed above.

Figures 8a and 8b illustrate the typical AFM topography images of undoped and 1 at% Ga-doped ZnO NRAs/P3HT films, respectively. The root mean square (RMS) surface roughness of P3HT coated on the undoped ZnO NRAs (7.26 nm) was smaller than that coated on the 1 at% Ga-doped ZnO NRAs (8.67 nm). The slightly increased RMS surface roughness reflects the longer ZnO NRAs located underneath the P3HT layer, which is in accordance with the FESEM results. Figure 9c and d show the corresponding surface potential images under dark and illumination conditions. The surface potential under illumination shifted positively compared to that in the dark, indicating an excess of positive charges on the surface of the P3HT.[43] The positive shift implies that the exciton dissociation occurs at the P3HT/ZnO interface and the generated electrons transport to FTO via ZnO NRAs, whereas the holes accumulate within the P3HT layer.[44,45] The surface potential shift (SP shift = $SP_{light} - SP_{dark}$) as a function of Ga concentration is shown in Figure 9. The SP shift became more pronounced when the Ga concentration increased from 0 (16

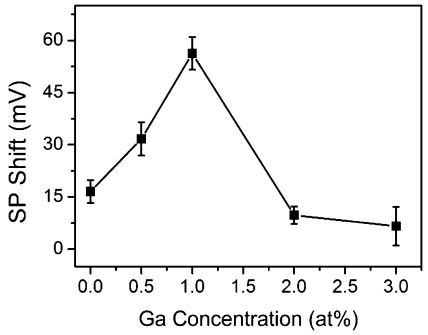

Figure 9. Surface potential shift under dark and illumination condition as a function of Ga concentration.

± 3 mV) to 1 at % (56 ± 5 mV), revealing the increase in accumulation of positive charges on the P3HT surface under illumination. This agrees well with the PL quenching and decay lifetime measurements, which indicate an improvement in exciton dissociation. However, the SP shift dropped significantly when the Ga concentration was further raised to 2 (9 ± 2 mV) and 3 at % (6 ± 5 mV). The poor exciton dissociation is responsible for the reduction of hole accumulation on the P3HT surface.

CELIV measurements were conducted in the dark to investigate the equilibrium charge carrier extraction characteristics. Figure 10 shows the current density responses for the FTO/ZnO NRAs/P3HT/Ag devices with different Ga doping concentrations. It is difficult to distinguish the electron and

dx.doi.org/10.1021/am5007832 | ACS Appl. Mater. Interfaces 2014, 6, 5308−5318

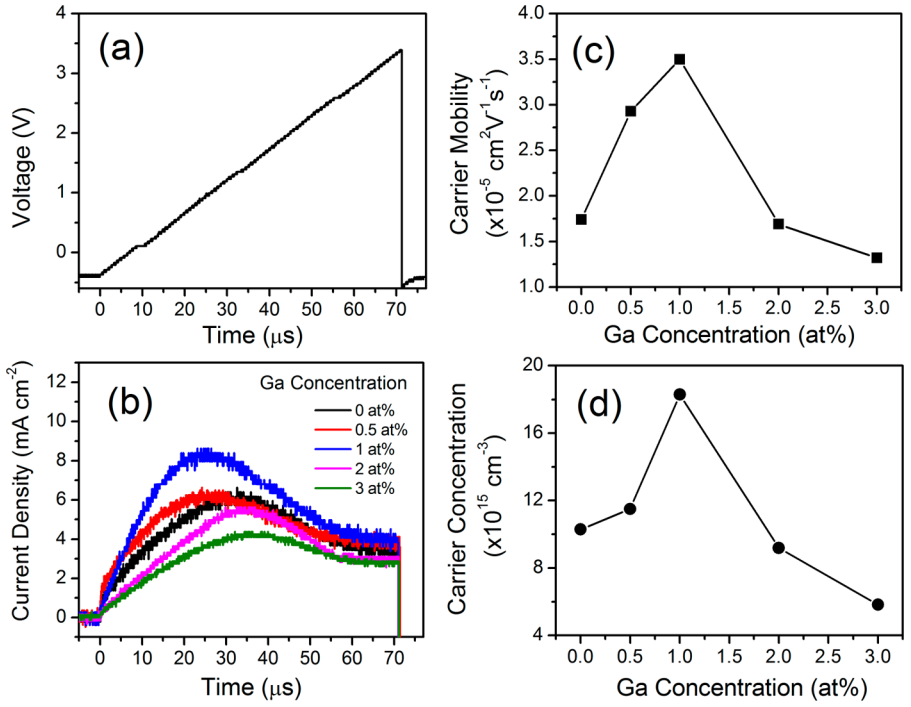

Figure 10. (a) Input pulse of the linearly increasing voltage with a slope of 0.05 V μs^{-1} for CELIV measurement. (b) Charge extraction response of devices with different Ga doping concentrations, (c) charge carrier mobility, and (d) equilibrium charge carrier concentration as a function of Ga doping concentration.

hole extraction from the CELIV measurement because neither contact was blocking in the present device structure.[46] The estimated charge carrier mobility (μ) was calculated using the equation $\mu = 2d^2/(3At_{max}^2[1 + 0.36(\Delta j/j(0))])$, where d is the thickness, A is the voltage slope, t_{max} is the time for extraction current reaching its maximum, Δj is the maximum extraction current, and $j(0)$ is the capacitive displacement current.[47] The charge carrier mobility increased from 1.94×10^{-5} to 3.5×10^{-5} cm^2 V^{-1} s^{-1} with increasing Ga concentration from 0 to 1 at %, as shown in Figure 10c. However, further increasing the Ga dopant concentration up to 3 at % leads to a lower carrier mobility of 1.32×10^{-5} cm^2 V^{-1} s^{-1}. The area under the current density versus time curve represents the total capacitive charges and equilibrium charge carrier extracted from the device. The extracted charge carrier concentration could be estimated by integrating the current density over the time.[26] It was found that the estimated charge carrier concentration of the 1 at % Ga-doped device (18.3×10^{15} cm^{-3}) was nearly two times larger than that of the undoped device (10.3×10^{15} cm^{-3}), as depicted in Figure 10d. The increase in extracted charge carriers could be attributed to the higher number of free charge carriers induced by the substitution of Ga^{3+} into the Zn^{2+} sites as well as the reduction of oxygen interstitials that trap the electrons. However, the extracted charge carrier concentration of the 3 at% Ga-doped device was the smallest. Apart from efficient exciton dissociation, the improved carrier mobility and charge carrier extraction also contribute to the improvement of J_{sc}.

It is generally accepted that the maximum achievable V_{oc} is governed by the difference between the conduction band edge of ZnO and the highest occupied molecular orbital (HOMO) of P3HT.[48] The optical band gaps of the ZnO NRAs with different Ga doping concentrations were estimated from the plot of $(\alpha h\nu)^2$ versus $h\nu$ (Figure 11), where α is the optical

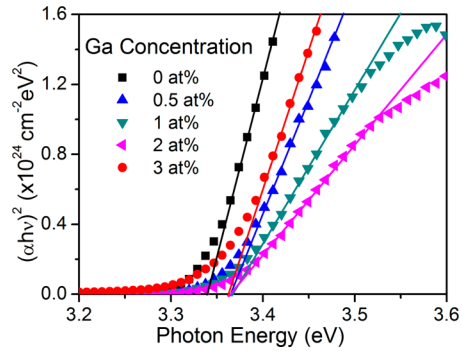

Figure 11. Plot of $(\alpha h\nu)^2$ versus photon energy for the ZnO NRAs with different Ga doping concentrations.

absorption coefficient, h is Planck's constant, and ν is the frequency of the incident photon. The optical band gap of the undoped ZnO NRAs shifted slightly from 3.33 to 3.36 eV when Ga dopants were introduced at concentrations of 0.5, 1, 2, and 3 at %. It has been previously reported that the incorporation of Ga into ZnO increases the carrier concentration as a result of one extra carrier created by the substitutional doping of Ga^{3+} into Zn^{2+} sites.[30] The lower energy state in the conduction band is filled by the extra carrier, blocking the transition from the valence band to that energy state. This leads to an upward shift of the conduction band edge toward vacuum level with increasing carrier concentration.[22] The increase in the Ga-doped ZnO conduction band edge as evidenced by the enlargement of the optical band gap could be one of the reasons for the V_{oc} improvement. However, it should be stressed that the V_{oc} began to decrease when the Ga concentration was increased to 2 and 3 at %. Therefore, the change in V_{oc} could not be simply attributed to the variation in

dx.doi.org/10.1021/am5007832 | ACS Appl. Mater. Interfaces 2014, 6, 5308−5318

the optical band gap; otherwise, the V_{oc} would be expected to increase with the Ga concentration up to 3 at %.

As seen in Figure 12, the dark $J-V$ curves reveal that the leakage (reverse bias) current decreased, whereas the forward bias current increased with increasing Ga concentration up to 1 at %. The opposite trend was observed when the concentration of Ga was increased to 2 and 3 at %. The dependence of the leakage and forward bias currents on the concentration of Ga was found to be similar to that of R_{sh} and R_s. It has been previously suggested that V_{oc} can be improved by reducing the leakage current.[20,49] The difference in leakage current could be attributed to the density of ZnO NRAs. For a Ga concentration in the range of 0 to 1 at %, the increased nanorod density could minimize the direct contact between the P3HT and FTO substrate, which was not fully covered by the ZnO nanoparticle seed layer.[20,50] As a result, the hole leakage current from the P3HT to the FTO could be reduced; thereby, a larger V_{oc} was obtained. As the Ga concentration was increased to greater than 1 at %, the density of the nanorods dropped significantly, as observed from the FESEM images (Figure 1). This, in turn, caused a larger contact area between the P3HT and FTO, resulting in a larger hole leakage current and a smaller V_{oc}. Meanwhile, the increased forward bias current and R_s correlate well with the reduction of oxygen interstitials and the introduction of extra free charge carriers as a result of Ga doping, which is in agreement with the CELIV measurements. The smallest R_s and the highest R_{sh} obtained at a Ga concentration of 1 at % resulted in the largest value of FF.

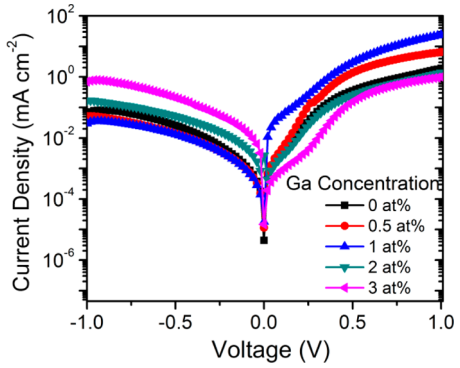

Figure 12. $J-V$ curves of devices with different Ga doping concentrations under dark conditions.

Impedance spectroscopy measurements have been widely used to investigate the charge transfer process at the interface of ZnO/P3HT.[14,20,51] Figure 13a shows a typical impedance spectrum of an undoped ZnO NRAs/P3HT device with a bias voltage of 0.25 V under dark conditions. The spectrum consists of a left semicircle in the high frequency region and a right semicircle in the low frequency region. The spectrum was fitted by an equivalent circuit model composed of two parallel combinations of resistance−capacitance ($R-C$) in series. The R_1-C_1 corresponding to the left semicircle is related to the geometric contribution of the bulk P3HT, whereas the R_2-C_2 corresponding to the right semicircle is attributed to the charge transfer process at the interface between the P3HT and ZnO NRAs.[52] To further understand the charge transfer process at the ZnO NRAs/P3HT interface, special emphasis was placed upon the extracted values of R_2 and C_2 as a function of the bias voltage for different Ga concentrations (Figure 13b and c). In general, the R_2 represents recombination resistance at the interface, whereas the C_2 is closely correlated with the accumulation of charge carriers at the interface.[52] The C_2 increased with increasing bias voltage up to a certain level, beyond which the C_2 was found to decrease gradually. This result suggests that more electrons and holes are injected from the FTO and Ag, respectively, followed by accumulation at the interface.[52] The electrons and holes are able to transport across the interface or undergo charge recombination at a relatively high bias voltage, resulting in reduced C_2. It should be noted that high density ZnO NRAs with a large surface area does not guarantee a large interfacial area between the ZnO and P3HT because the infiltration of P3HT is highly dependent on the spacing between the ZnO nanorods.[14] Interestingly, the highest value of C_2 was achieved at a Ga concentration of 1 at %, in which the highest-density ZnO NRAs were obtained. This result indirectly suggests that the P3HT could infiltrate well into the interspacing of the ZnO NRAs and create a larger interfacial area for charge transfer processes. In contrast to C_2, the R_2 decreased with increasing bias voltage in the tested range, indicating that the charge recombination is enhanced at higher bias voltages.[51] It is worth noting that the 1 at % Ga-doped device exhibited the highest value of R_2, which implies that the charge recombination across the 1 at % Ga-doped ZnO NRAs/P3HT interfaces can be significantly reduced.

It should be noted that the V_{oc} is also dependent on the difference between quasi-Fermi levels of electrons in the ZnO and holes in the P3HT.[39,53,54] Generally, the increase in photogenerated free charge carriers enlarges the quasi-Fermi level separation, thus leading to a larger V_{oc}. To investigate the charge recombination dynamics of the device under open circuit voltage conditions, transient photovoltage decay measurements were employed. Figure 14 demonstrates the photovoltage decay curves of the devices with various Ga concentrations. The additional electrons and holes generated by the light pulse can only undergo recombination across the

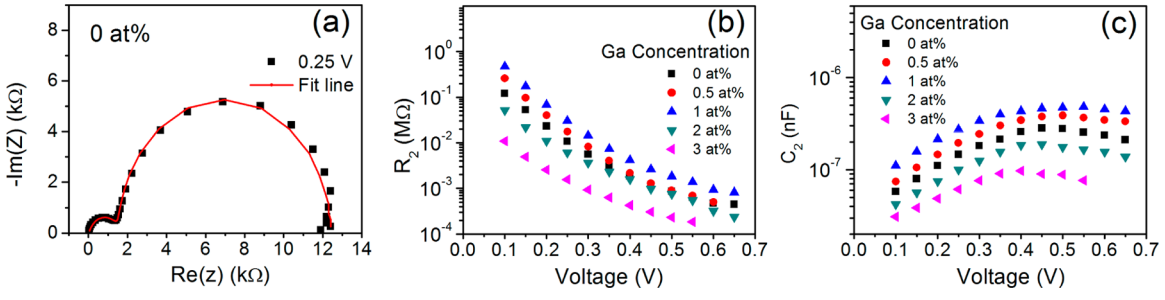

Figure 13. (a) Impedance spectrum of the undoped ZnO/P3HT device at 0.25 V. Extracted values of (b) R_2 and (c) C_2 as a function of bias voltage for devices with different Ga doping concentrations under dark conditions.

dx.doi.org/10.1021/am5007832 | ACS Appl. Mater. Interfaces 2014, 6, 5308−5318

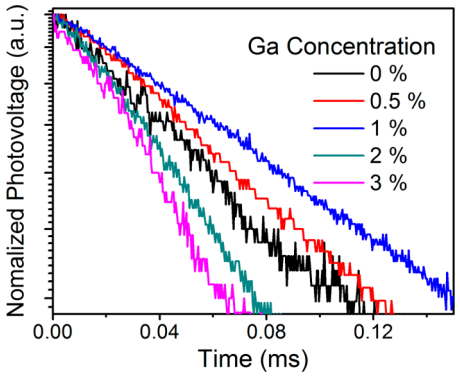

Figure 14. Photovoltage decay curves of the devices with different Ga concentrations under open circuit conditions.

interface because there is no current flow under open circuit conditions.[27] The lifetime of photovoltage decay is governed by the rate of recombination of those extra free charge carriers. The curve was fitted with a single exponential decay function to estimate the charge recombination lifetime.[27] The recombination lifetime of the undoped device increased significantly from 98 to 162 μs for the 1 at % Ga-doped ZnO NRAs device. It is believed that the reduction of oxygen interstitials, which trap the electrons on ZnO NRAs, is responsible for the increased recombination lifetime. The increase in the recombination lifetime leads to increased electron and hole concentrations and thus a larger difference between the quasi-Fermi levels of the electrons in ZnO and the holes in P3HT. However, relatively poor recombination lifetimes of 75 and 57 μs were observed for the 2 and 3 at % Ga-doped devices, respectively. The relatively high doping level of Ga might adversely affect the grain growth in individual ZnO nanorods, leading to poor crystallinity.[55,56] As a result, the defects induced by the Ga doping could serve as recombination centers, which would subsequently promote the recombination process.[22] The correlation between the recombination lifetime and the Ga concentration was found to be in agreement with the impedance spectroscopy measurements described above. Aside from the reduced leakage current, the suppression of charge recombination is considered a key factor in improving the V_{oc}, particularly at a Ga concentration of 1 at %.

Despite the significant improvements in the photovoltaic performance achieved by Ga doping, the devices with Ga-doped ZnO NRAs as electron acceptors still exhibited much lower PCE values compared to the devices based on P3HT and PCBM, likely as a result of poor compatibility between the hydrophilic ZnO and the hydrophobic P3HT.[17] It has been reported that the compatibility between ZnO and P3HT could be enhanced via interface molecular modification on the ZnO surface, resulting in a more efficient exciton dissociation and higher PCE.[57] In addition, it is believed that the photovoltaic performance of the present devices could be further improved by inserting an interlayer between the active layer and the top electrodes,[58] minimizing the electron leakage current.

CONCLUSIONS

Long, small-diameter, and high-density ZnO NRAs with low oxygen defects have been successfully synthesized by controlling the doping concentration of Ga. The photovoltaic performance of OSCs using these Ga-doped ZnO NRAs as electron acceptors has been investigated. The J_{sc} and V_{oc} increased with increasing Ga concentration up to an optimum concentration of 1 at %. The improvement of J_{sc} is attributed to the enhanced exciton dissociation and charge extraction, whereas the increased V_{oc} correlates to the reduced charge recombination and hole leakage current. It is interesting to note that the PCE of the device with optimum Ga concentration increased by nearly three times compared to that of the undoped device. The doping of Ga has been demonstrated to be a simple and effective approach to improve the photovoltaic performance of OSCs.

AUTHOR INFORMATION

Corresponding Author

*E-mail: ccyap@ukm.my.

Notes

The authors declare no competing financial interest.

ACKNOWLEDGMENTS

This work has been conducted under the financial support of Universiti Kebangsaan Malaysia under Research Grant DLP-2013-40. The authors would like to thank Mr. Idris Zulkifle from the School of Applied Physics, Universiti Kebangsaan Malaysia for Ag sputtering. The authors would also like to acknowledge Mr. Muhammad Nazrul Zahari from the Centre for Research & Instrumentation Management, Universiti Kebangsaan Malaysia for AFM characterization.

REFERENCES

(1) Krebs, F. C.; Jørgensen, M.; Norrman, K.; Hagemann, O.; Alstrup, J.; Nielsen, T. D.; Fyenbo, J.; Larsen, K.; Kristensen, J. A Complete Process for Production of Flexible Large Area Polymer Solar Cells Entirely using Screen Printing-First Public Demonstration. *Sol. Energy Mater. Sol. Cells* **2009**, *93*, 422−441.

(2) Krebs, F. C.; Jørgensen, M. Polymer and Organic Solar Cells Viewed as Thin Film Technologies: What it Will Take for Them to Become a Success Outside Academia. *Sol. Energy Mater. Sol. Cells* **2013**, *119*, 73−76.

(3) Dennler, G.; Scharber, M. C.; Brabec, C. J. Polymer-Fullerene Bulk-Heterojunction Solar Cells. *Adv. Mater.* **2009**, *21*, 1323−1338.

(4) Khelifi, S.; Voroshazi, E.; Spoltore, D.; Piersimoni, F.; Bertho, S.; Aernouts, T.; Manca, J.; Lauwaert, J.; Vrielinck, H.; Burgelman, M. Effect of Light Induced Degradation on Electrical Transport and Charge Extraction in Polythiophene:Fullerene (P3HT:PCBM) Solar Cells. *Sol. Energy Mater. Sol. Cells* **2014**, *120* (PartA), 244−252.

(5) Cheng, C.-E.; Pei, Z.; Hsu, C.-C.; Chang, C.-S.; Shih-Sen Chien, F. Hole Transit in P3HT:PCBM Solar Cells with Embedded Gold Nanoparticles. *Sol. Energy Mater. Sol. Cells* **2014**, *121*, 80−84.

(6) Yang, X.; Loos, J. Toward High-Performance Polymer Solar Cells: The Importance of Morphology Control. *Macromolecules* **2007**, *40*, 1353−1362.

(7) Tremolet de Villers, B.; Tassone, C. J.; Tolbert, S. H.; Schwartz, B. J. Improving the Reproducibility of P3HT:PCBM Solar Cells by Controlling the PCBM/Cathode Interface. *J. Phys. Chem. C* **2009**, *113*, 18978−18982.

(8) Zhao, J.; Swinnen, A.; Van Assche, G.; Manca, J.; Vanderzande, D.; Mele, B. V. Phase Diagram of P3HT/PCBM Blends and Its Implication for the Stability of Morphology. *J. Phys. Chem. B* **2009**, *113*, 1587−1591.

(9) Treat, N. D.; Brady, M. A.; Smith, G.; Toney, M. F.; Kramer, E. J.; Hawker, C. J.; Chabinyc, M. L. Interdiffusion of PCBM and P3HT Reveals Miscibility in Photovoltaically Active Blend. *Adv. Energy Mater.* **2011**, *1*, 82−89.

(10) Olson, D. C.; Piris, J.; Collins, R. T.; Shaheen, S. E.; Ginley, D. S. Hybrid Photovoltaic Devices of Polymer and ZnO Nanofiber Composites. *Thin Solid Films* **2006**, *496*, 26−29.

(11) Olson, D. C.; Lee, Y.-J.; White, M. S.; Kopidakis, N.; Shaheen, S. E.; Ginley, D. S.; Voigt, J. A.; Hsu, J. W. Effect of Polymer Processing on the Performance of Poly (3-hexylthiophene)/ZnO Nanorod Photovoltaic Devices. *J. Phys. Chem. C* **2007**, *111*, 16640−16645.
(12) Olson, D. C.; Shaheen, S. E.; Collins, R. T.; Ginley, D. S. The Effect of Atmosphere and ZnO Morphology on the Performance of Hybrid Poly(3-hexylthiophene)/ZnO Nanofiber Photovoltaic Devices. *J. Phys. Chem. C* **2007**, *111*, 16670−16678.
(13) Takanezawa, K.; Hirota, K.; Wei, Q.-S.; Tajima, K.; Hashimoto, K. Efficient Charge Collection with ZnO Nanorod Array in Hybrid Photovoltaic Devices. *J. Phys. Chem. C* **2007**, *111*, 7218−7223.
(14) Conings, B.; Baeten, L.; Boyen, H.-G.; D'Haen, J.; Van Bael, M. K.; Manca, J. V. Relation between Morphology and Recombination Kinetics in Nanostructured Hybrid Solar Cells. *J. Phys. Chem. C* **2012**, *116*, 14237−14242.
(15) Kudo, N.; Honda, S.; Shimazaki, Y.; Ohkita, H.; Ito, S.; Benten, H. Improvement of Charge Injection Efficiency in Organic−Inorganic Hybrid Solar Cells by Chemical Modification of Metal Oxides with Organic Molecules. *Appl. Phys. Lett.* **2007**, *90*, No. 183513.
(16) Ruankham, P.; Sagawa, T.; Sakaguchi, H.; Yoshikawa, S. Vertically Aligned ZnO Nanorods Doped with Lithium for Polymer Solar Cells: Defect Related Photovoltaic Properties. *J. Mater. Chem.* **2011**, *21*, 9710−9715.
(17) Chen, C.-T.; Hsu, F.-C.; Sung, Y.-M.; Liao, H.-C.; Yen, W.-C.; Su, W.-F.; Chen, Y.-F. Effects of Metal-Free Conjugated Oligomer as a Surface Modifier in Hybrid Polymer/ZnO Solar Cells. *Sol. Energy Mater. Sol. Cells* **2012**, *107*, 69−74.
(18) Zhao, Q.; Yang, L.-L.; Willander, M.; Sernelius, B. E.; Holtz, P. Surface Recombination in ZnO Nanorods Grown by Chemical Bath Deposition. *J. Appl. Phys.* **2008**, *104*, No. 073526.
(19) Yang, L. L.; Zhao, Q. X.; Willander, M.; Liu, X. J.; Fahlman, M.; Yang, J. H. Origin of the Surface Recombination Centers in ZnO Nanorods Arrays by X-ray Photoelectron Spectroscopy. *Appl. Surf. Sci.* **2010**, *256*, 3592−3597.
(20) Ginting, R. T.; Yap, C. C.; Yahaya, M.; Mat Salleh, M. Improvement of Inverted Type Organic Solar Cells Performance by Incorporating Mg Dopant into Hydrothermally Grown ZnO Nanorod Arrays. *J. Alloy Compd.* **2014**, *585*, 696−702.
(21) Shin, K.-S.; Lee, K.-H.; Lee, H. H.; Choi, D.; Kim, S.-W. Enhanced Power Conversion Efficiency of Inverted Organic Solar Cells with a Ga-Doped ZnO Nanostructured Thin Film Prepared Using Aqueous Solution. *J. Phys. Chem. C* **2010**, *114*, 15782−15785.
(22) Shin, K.-S.; Park, H.-J.; Yoon, G. C.; Jeong, S.-W.; Kumar, B.; Kim, S.-W. Doping Effect of Electron Transport Layer on Nanoscale Phase Separation and Charge Transport in Bulk Heterojunction Solar Cells. *J. Phys. Chem. C* **2013**, *117*, 24692−24699.
(23) Thambidurai, M.; Kim, J. Y.; Song, J.; Ko, Y.; Song, H.-j.; Kang, C.-m.; Muthukumarasamy, N.; Velauthapillai, D.; Lee, C. High Performance Inverted Organic Solar Cells with Solution Processed Ga-Doped ZnO as an Interfacial Electron Transport Layer. *J. Mater. Chem. C* **2013**, *1*, 8161−8166.
(24) Vayssieres, L. Growth of Arrayed Nanorods and Nanowires of ZnO from Aqueous Solutions. *Adv. Mater.* **2003**, *15*, 464−466.
(25) Greene, L. E.; Law, M.; Goldberger, J.; Kim, F.; Johnson, J. C.; Zhang, Y.; Saykally, R. J.; Yang, P. Low-Temperature Wafer-Scale Production of ZnO Nanowire Arrays. *Angew. Chem., Int. Ed.* **2003**, *42*, 3031−3034.
(26) Pivrikas, A.; Sariciftci, N.; Juška, G.; Österbacka, R. A Review of Charge Transport and Recombination in Polymer/Fullerene Organic Solar Cells. *Prog. Photovoltaics Res. Appl.* **2007**, *15*, 677−696.
(27) Shuttle, C. G.; O'Regan, B.; Ballantyne, A. M.; Nelson, J.; Bradley, D. D. C.; de Mello, J.; Durrant, J. R. Experimental Determination of the Rate Law for Charge Carrier Decay in a Polythiophene: Fullerene Solar Cell. *Appl. Phys. Lett.* **2008**, *92*, No. 093311.
(28) Wang, H.; Baek, S.; Song, J.; Lee, J.; Lim, S. Microstructural and Optical Characteristics of Solution-Grown Ga-Doped ZnO Nanorod Arrays. *Nanotechnology* **2008**, *19*, 075607.
(29) Phan, D.-T.; Chung, G.-S. Effects of Defects in Ga-Doped ZnO Nanorods Formed by a Hydrothermal Method on CO Sensing Properties. *Sens. Actuators, B* **2013**, *187*, 191−197.
(30) Park, G. C.; Hwang, S. M.; Choi, J. H.; Kwon, Y. H.; Cho, H. K.; Kim, S.-W.; Lim, J. H.; Joo, J. Effects of In or Ga Doping on the Growth Behavior and Optical Properties of ZnO Nanorods Fabricated by Hydrothermal Process. *Phys. Status Solidi A* **2013**, *210*, 1552−1556.
(31) Shannon, R. D. Revised Effective Ionic Radii and Systematic Studies of Interatomic Distances in Halides and Chalcogenides. *Acta Crystallogr. A* **1976**, *32*, 751−767.
(32) Mekki, A.; Tabet, N.; Hezam, M. Synthesis and Characterisation of Nitrogen-Doped ZnO Thin Films. *Int. J. Nano Biomater.* **2009**, *2*, 216−225.
(33) Chen, M.; Wang, X.; Yu, Y.; Pei, Z.; Bai, X.; Sun, C.; Huang, R.; Wen, L. X-ray Photoelectron Spectroscopy and Auger Electron Spectroscopy Studies of Al-Doped ZnO Films. *Appl. Surf. Sci.* **2000**, *158*, 134−140.
(34) Cao, H. T.; Pei, Z. L.; Gong, J.; Sun, C.; Huang, R. F.; Wen, L. S. Preparation and Characterization of Al and Mn Doped ZnO (ZnO: (Al, Mn)) Transparent Conducting Oxide Films. *J. Solid State Chem.* **2004**, *177*, 1480−1487.
(35) Fan, J. C. C.; Goodenough, J. B. X-ray Photoemission Spectroscopy Studies of Sn-Doped Indium-Oxide Films. *J. Appl. Phys.* **1977**, *48*, 3524−3531.
(36) Islam, M. N.; Ghosh, T. B.; Chopra, K. L.; Acharya, H. N. XPS and X-ray Diffraction Studies of Aluminum-Doped Zinc Oxide Transparent Conducting Films. *Thin Solid Films* **1996**, *280*, 20−25.
(37) Cross, R.; De Souza, M.; Narayanan, E. S. A Low Temperature Combination Method for the Production of ZnO Nanowires. *Nanotechnology* **2005**, *16*, 2188.
(38) Kim, Y.; Cook, S.; Tuladhar, S. M.; Choulis, S. A.; Nelson, J.; Durrant, J. R.; Bradley, D. D.; Giles, M.; McCulloch, I.; Ha, C.-S. A Strong Regioregularity Effect in Self-Organizing Conjugated Polymer Films and High-Efficiency Polythiophene: Fullerene Solar Cells. *Nat. Mater.* **2006**, *5*, 197−203.
(39) Lin, Y.-Y.; Lee, Y.-Y.; Chang, L.; Wu, J.-J.; Chen, C.-W. The Influence of Interface Modifier on the Performance of Nanostructured ZnO/Polymer Hybrid Solar Cells. *Appl. Phys. Lett.* **2009**, *94*, 063308−063308-3.
(40) Chen, J.-Y.; Hsu, F.-C.; Sung, Y.-M.; Chen, Y.-F. Enhanced Charge Transport in Hybrid Polymer/ZnO-Nanorod Solar Cells Assisted by Conductive Small Molecules. *J. Mater. Chem.* **2012**, *22*, 15726−15731.
(41) Elumalai, N. K.; Jin, T. M.; Chellappan, V.; Jose, R.; Palaniswamy, S. K.; Jayaraman, S.; Raut, H. K.; Ramakrishna, S. Electrospun ZnO Nanowire Plantations in the Electron Transport Layer for High-Efficiency Inverted Organic Solar Cells. *ACS Appl. Mater. Interfaces* **2013**, *5*, 9396−9404.
(42) Weickert, J.; Auras, F.; Bein, T.; Schmidt-Mende, L. Characterization of Interfacial Modifiers for Hybrid Solar Cells. *J. Phys. Chem. C* **2011**, *115*, 15081−15088.
(43) Zeng, T.-W.; Hsu, F.-C.; Tu, Y.-C.; Lin, T.-H.; Su, W.-F. Kelvin Probe Force Microscopy Study on Hybrid P3HT: Titanium Dioxide Nanorod Materials. *Chem. Phys. Lett.* **2009**, *479*, 105−108.
(44) Sung, Y.-M.; Hsu, F.-C.; Wang, D.-Y.; Wang, I.-S.; Chen, C.-C.; Liao, H.-C.; Su, W.-F.; Chen, Y.-F. Enhanced Charge Extraction in Inverted Hybrid Photovoltaic Cells Assisted by Graphene Nanoflakes. *J. Mater. Chem.* **2011**, *21*, 17462−17467.
(45) Chen, C.-T.; Hsu, F.-C.; Sung, Y.-M.; Liao, H.-C.; Yen, W.-C.; Su, W.-F.; Chen, Y.-F. Effects of Metal-Free Conjugated Oligomer as a Surface Modifier in Hybrid Polymer/ZnO Solar Cells. *Sol. Energy Mater. Sol. Cells* **2012**, *107*, 69−74.
(46) Kumar, A.; Liao, H.-H.; Yang, Y. Hole Mobility in Optimized Organic Photovoltaic Blend Films Obtained using Extraction Current Transients. *Org. Electron.* **2009**, *10*, 1615−1620.
(47) Juška, G.; Arlauskas, K.; Viliūnas, M.; Genevičius, K.; Österbacka, R.; Stubb, H. Charge Transport in π-Conjugated Polymers from Extraction Current Transients. *Phys. Rev. B* **2000**, *62*, R16235.

(48) Nagata, T.; Oh, S.; Yamashita, Y.; Yoshikawa, H.; Ikeno, N.; Kobayashi, K.; Chikyow, T.; Wakayama, Y. Photoelectron Spectroscopic Study of Band Alignment of Polymer/ZnO Photovoltaic Device Structure. *Appl. Phys. Lett.* **2013**, *102*, No. 043302.
(49) Itoh, E.; Goto, Y.; Fukuda, K. Bulk-Heterojunction Organic Solar Cells Sandwiched by Solution Processed Molybdenum Oxide and Titania Nanosheet Layers. *Jpn. J. Appl. Phys.* **2014**, *53*, No. 02BE08.
(50) Ravirajan, P.; Peiró, A. M.; Nazeeruddin, M. K.; Graetzel, M.; Bradley, D. D. C.; Durrant, J. R.; Nelson, J. Hybrid Polymer/Zinc Oxide Photovoltaic Devices with Vertically Oriented ZnO Nanorods and an Amphiphilic Molecular Interface Layer. *J. Phys. Chem. B* **2006**, *110*, 7635−7639.
(51) Wu, S.; Tai, Q.; Yan, F. Hybrid Photovoltaic Devices Based on Poly (3-hexylthiophene) and Ordered Electrospun ZnO Nanofibers. *J. Phys. Chem. C* **2010**, *114*, 6197−6200.
(52) Conings, B.; Baeten, L.; Boyen, H.-G.; Spoltore, D.; D'Haen, J.; Grieten, L.; Wagner, P.; Van Bael, M. K.; Manca, J. V. Influence of Interface Morphology onto the Photovoltaic Properties of Nanopatterned ZnO/Poly(3-hexylthiophene) Hybrid Solar Cells. An Impedance Spectroscopy Study. *J. Phys. Chem. C* **2011**, *115*, 16695−16700.
(53) Li, S.-S.; Lin, Y.-Y.; Su, W.-F.; Chen, C.-W. Polymer/Metal Oxide Nanocrystals Hybrid Solar Cells. *IEEE J. Sel. Top. Quant.* **2010**, *16*, 1635−1640.
(54) Yip, H.-L.; Jen, A. K. Y. Recent Advances in Solution-Processed Interfacial Materials for Efficient and Stable Polymer Solar Cells. *Energ. Environ. Sci.* **2012**, *5*, 5994−6011.
(55) Elumalai, N. K.; Vijila, C.; Jose, R.; Zhi Ming, K.; Saha, A.; Ramakrishna, S. Simultaneous Improvements in Power Conversion Efficiency and Operational Stability of Polymer Solar Cells by Interfacial Engineering. *Phys. Chem. Chem. Phys.* **2013**, *15*, 19057−19064.
(56) Archana, P. S.; Jose, R.; Jin, T. M.; Vijila, C.; Yusoff, M. M.; Ramakrishna, S. Structural and Electrical Properties of Nb-Doped Anatase TiO_2 Nanowires by Electrospinning. *J. Am.. Ceram. Soc.* **2010**, *93*, 4096−4102.
(57) Ruankham, P.; Yoshikawa, S.; Sagawa, T. Effects of the Morphology of Nanostructured ZnO and Interface Modification on the Device Configuration and Charge Transport of ZnO/Polymer Hybrid Solar Cells. *Phys. Chem. Chem. Phys.* **2013**, *15*, 9516−9522.
(58) Wang, M.; Li, Y.; Huang, H.; Peterson, E. D.; Nie, W.; Zhou, W.; Zeng, W.; Huang, W.; Fang, G.; Sun, N.; Zhao, X.; Carroll, D. L. Thickness Dependence of the MoO3 Blocking Layers on ZnO Nanorod-Inverted Organic Photovoltaic Devices. *Appl. Phys. Lett.* **2011**, *98*, No. 103305.